Quantitative measure of topological protection in Floquet systems through the spectral localizer

Stephan Wong [1,*] Alexander Cerjan [1,†] and Justin T. Cole [2,‡]

[1] *Center for Integrated Nanotechnologies, Sandia National Laboratories, Albuquerque, New Mexico 87185, USA*

[2] *Department of Mathematics, University of Colorado, Colorado Springs, Colorado 80918, USA*

(Received 1 November 2024; revised 19 September 2025; accepted 6 November 2025; published 8 December 2025)

The standard understanding of topological protection from band theory is that a system's topology cannot change without first closing the bulk band gap. However, in Floquet systems, this typical definition of topological protection is one step removed from the experimentally accessible system parameters, as the relationship between the disorder in a system's instantaneous Hamiltonian and its Floquet Hamiltonian that defines its topology is not straightforward. Here, we demonstrate that the spectral localizer framework for classifying material topology can be applied to Floquet systems using solely the Floquet Hamiltonian and prove that its associated measure of topological protection can be understood in terms of the disorder across the system's instantaneous Hamiltonians. As such, we have derived a quantitative bound on a Floquet system's topological protection in terms of the instantaneous system. Moreover, we show the utility of these bounds in both ordinary and anomalous Floquet Chern insulators.

DOI: 10.1103/3y9q-jpbm

I. INTRODUCTION

In recent years, photonic Chern insulators have excited the photonics community due to their potential to yield robust wavelength-scale nonreciprocal devices, such as isolators and circulators. While early work in realizing photonic Chern insulators utilized gyro-optical materials [1], shifted ring resonators [2,3], and exciton-polariton lattices [4] to break, or effectively break, time-reversal symmetry, these platforms have yet to realize the full promise of wavelength-scale devices for nanophotonics applications, either because the magneto-optic effect is too weak at telecommunication wavelengths [5–7] or because of the need for highly structured metasurfaces negates the flexibility provided by topological robustness against fabrication defects. These challenges can instead be circumvented through the use of alternative approaches for breaking time-reversal symmetry; for example, it is possible to realize photonic Chern insulators by periodically driving an otherwise trivial system [8–13]. In particular, such topological Floquet systems have been proposed and experimentally demonstrated in helical waveguides array mimicking a time-periodic Hamiltonian [14–22] or with periodically pump-driven lithium niobate photonic crystals [23].

However, the characterization of topology in Floquet systems differs from that in static systems, as the system's time evolution must be incorporated into the classification framework. Previously, the Floquet Hamiltonian, derived from the evolution operator, has been used to classify the topology of driven or otherwise time-periodic systems using tools from topological band theory [24]. Nevertheless, although the Floquet Hamiltonian can be used to identify topologically nontrivial modes through its spectrum, topological band theory has been shown to be inadequate to correctly capture the topology in the topological anomalous Floquet modes, as the associated Floquet bands have trivial Chern numbers [25]. To fully characterize the topology in Floquet systems, subsequent studies have argued that one needs to consider the full time evolution of the unitary propagator [26–28] or work with the time-reciprocal space Floquet Hamiltonian [25]. While there have been studies into the effects of disorder in Floquet systems [29,30], these methods have yet to analytically resolve the robustness of topological modes in the presence of both spatial disorder and variations in the driving protocol. Moreover, the use of a Floquet Hamiltonian to identify a system's topology obscures the effects of any topological protection. Although topological band theory predicts that a system's topology can change only if sufficient perturbations are added to close the associated band gap, the Floquet bands of a driven system are abstracted from the instantaneous Hamiltonians that can be controlled in experiments. Thus relating a quantitative definition of topological protection of Floquet systems to experimentally accessible parameters remains an outstanding challenge.

Here we propose a framework based on the spectral localizer to diagnose the topology in Floquet systems directly from the Floquet Hamiltonian and derive a bound for a system's topological protection in terms of perturbations to the system's associated time-dependent instantaneous Hamiltonian. As the spectral localizer is able to capture the topology of any edge modes present in a spectrum, we demonstrate that the spectral localizer can also correctly identify the topology of the edge modes present in the Floquet bands, even if the system is an anomalous Floquet insulator. In particular, we demonstrate that the correct characterization of the topology in Floquet systems is possible solely with the Floquet

*Contact author: stewong@sandia.gov

†Contact author: awcerja@sandia.gov

‡Contact author: jcole13@uccs.edu

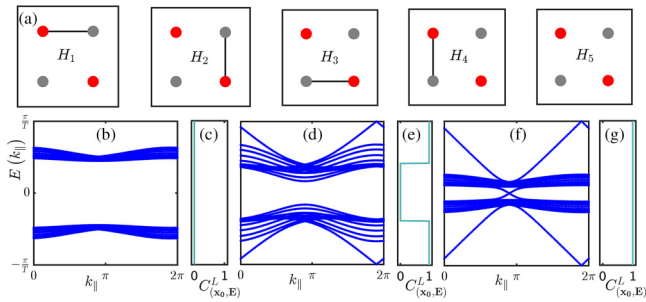

FIG. 1. (a) One period (five subintervals) of the driving protocol. Two sublattices are highlighted: gray dots (a sites) and red dots (b sites). Interactions of amplitude J in the first four subintervals are indicated by lines; there is no hopping in the last subinterval. Over each subinterval a detuning term $\mp\Delta = \mp\frac{\pi}{2T}$ is applied to the a, b sites, respectively. (Bottom row) As the hopping amplitude increases, left to right, the system transitions from a trivial to anomalous Chern insulator. The bulk bands and the corresponding local index $C^{\mathrm{L}}_{(\mathbf{x}_0,E)}$ given in Eq. (6) are shown for (b),(c)$J = \frac{\pi}{2T}$, (d),(e) $J = \frac{3\pi}{2T}$, and (f),(g) $J = \frac{5\pi}{2T}$. The local Chern number has been calculating at the center $\boldsymbol{x_0}$ of a 10×10 lattice, with $\kappa = 0.5/(Ta)$, period $T = 1$[a.u.], and lattice constant $a = 1$[a.u.].

Hamiltonian, contrary to previous claims in the literature [26–28]. Moreover, the local gap, which is a local and quantitative measure of the topological protection associated to the local topological markers obtained from the spectral localizer, provides insight into possible bounds on the spatial and temporal perturbation of the periodic driving protocol to preserve the nontrivial topology of the system. Overall, our classification framework lays out a general picture of the topology in Floquet systems that can be directly related to the spectral localizer framework for static systems [31–36] and provides insight into how careful the driving protocol should be in terms of perturbations. We anticipate that the platform agnostic feature of the Floquet spectral localizer framework, including its ability to probe local topology and the associated quantitative measure of topological protection, will be useful for experimental realizations of periodically driven photonic systems [14,16,17,22], as well as for driven nonlinear systems [19–21,23,35].

II. FLOQUET SPECTRAL LOCALIZER

To illustrate how the spectral localizer framework can be applied to Floquet systems, we consider a standard system described by a five-step driving protocol on a square lattice [25], as summarized in Fig. 1(a), with coupling strength J and detuning mass term $\mp\Delta$ applied to the a and b sublattice sites, respectively. As the coupling amplitude increases, the system goes through two topological transitions: from a trivial insulator to a Chern insulator, then from a Chern insulator to an anomalous Chern insulator, as shown by the existence or absence of edge states in the projected quasienergy bands in Figs. 1(b), 1(d), and 1(f). However, the bulk-edge correspondence from topological band theory is seemingly violated, because the bulk Chern number of the bands derived from the corresponding Floquet Bloch modes is unable to distinguish between the trivial and anomalous Chern insulators, with both band invariants being zero.

Instead, the topology of Floquet systems can be classified by generalizing the spectral localizer framework [37]. The key advantage of this approach is that the spectral localizer takes an operator-based methodology to establishing topology and as such is able to classify the local topology of any effective Hamiltonian and predict the existence (or absence) of topological protected modes regardless of the peculiarity of the system [31,32,34,36,38–40]. In particular, consider a Floquet system

$$i\frac{d\mathbf{u}}{dt} = H(t)\mathbf{u}(t), \tag{1}$$

characterized by a $N \times N$ Hermitian Hamiltonian that is T periodic $H(t+T) = H(t)$. The general solution of Eq. (1) is given by $\mathbf{u}(t) = \Pi(t, t_0)\mathbf{u}(t_0)$, where $\Pi(t, t_0)$ is the unitary evolution operator that can be expressed as $\Pi(t, t_0) = P(t, t_0)\exp[-i(t-t_0)H_{\mathrm{F}}]$ such that $P(t+T, t_0) = P(t, t_0)$ and $P(t_0, t_0) = I$ (identity) [41]. In practice, given linearly independent solutions $u_i(t)$, $i = 1, \ldots, N$ of Eq. (1), the unitary evolution operator (matrix solution) can be written as

$$\Pi(t, t_0) = [u_1(t)|\ldots|u_N(t)] \tag{2}$$

and, in the special case of n piecewise constant subintervals, $\Pi(t, t_0)$ is simply the product of exponentials

$$\begin{aligned}\Pi(t_n, t_0) &= \Pi(t_n, t_{n-1})\cdots\Pi(t_2, t_1)\Pi(t_1, t_0) \\ &= e^{-i(t_n - t_{n-1})H_n}\cdots e^{-i(t_2-t_1)H_2}e^{-i(t_1-t_0)H_1}.\end{aligned} \tag{3}$$

For such Floquet systems, the effective Hamiltonian can be chosen to be the Floquet Hamiltonian H_{F}, obtained from the evolution operator after one period, i.e., the monodromy matrix $\Pi(t_0 + T, t_0) = \exp(-iTH_{\mathrm{F}})$, as [42]

$$H_{\mathrm{F}} = -\frac{\log\Pi(t_0+T, t_0)}{iT}. \tag{4}$$

The Floquet Hamiltonian is a Hermitian matrix (see Appendix G), whose spectrum defines quasienergy bands that are similar to energy bands in the static Hamiltonian, but unique only up to integer shifts of $2\pi/T$. Compared to the instantaneous Hamiltonian $H(t)$, a system's Floquet Hamiltonian H_{F} contains enough information about the periodic time evolution in its quasienergy bands to enable the identification of a system's bulk and edge mode dispersion [24,25].

To diagnose the local topology of a two-dimensional Floquet system in class A [43–46] at specific location (x, y) and quasienergy E, the spectral localizer combines the Floquet Hamiltonian H_{F} along with the position operators X and Y as

$$\begin{aligned}&L_{(x,y,E)}(X, Y, H_{\mathrm{F}}) \\ &= \begin{pmatrix} (H_{\mathrm{F}} - EI) & \kappa(X - xI) - i\kappa(Y - yI) \\ \kappa(X - xI) + i\kappa(Y - yI) & -(H_{\mathrm{F}} - EI)\end{pmatrix},\end{aligned} \tag{5}$$

such that the system's local Chern number is given by

$$C^{\mathrm{L}}_{(x,y,E)}(X, Y, H_{\mathrm{F}}) = \tfrac{1}{2}\mathrm{sig}(L_{(x,y,E)}(X, Y, H_{\mathrm{F}})) \in \mathbb{Z}, \tag{6}$$

where the signature sig of a matrix is its number of positive eigenvalues minus its number of negative eigenvalues.

In Eq. (5), $\kappa > 0$ is a hyperparameter used to make units consistent between the position and Hamiltonian operators as well as to balance the spectral weight between positions and energy, and is typically of the order of $\kappa \sim E_{\text{gap}}/L$ [33,34,47], where E_{gap} is the relevant spectral gap and L the length of the finite system considered (see Appendix C for more discussion). Moreover, depending on the system's dimension and the local symmetry of its Floquet Hamiltonian H_{F} relative to the ten Altland-Zirnbauer classes [43–46], the spectral localizer can take different explicit formulations and the system's local topology at specific location and energy is given by either the signature or the sign of the determinant or the Pfaffian of the spectral localizer [37,48].

A few technical comments are appropriate concerning the multivaluedness of the Floquet Hamiltonian in Eq. (4) [49] and thus of the spectral localizer. In particular, here, we take the principal branch cut along the negative real axis so that $-i\log e^{i\theta} = \theta$ for $\theta \in [-\pi, \pi)$. While nontrivial topological phases can arise from the interaction of the Floquet bands across multiple Floquet branches [25], a specific choice of the branch will not alter the topological phase. Given a topological band gap around E, that gap also exists at $E + m2\pi/T$ with $m \in \mathbb{Z}$, i.e., at a different branch, with the same gap width and topology, as shifting the spectrum by $m2\pi/T$ from one branch to another will not induce any band inversions responsible for changing of topology. Moreover, for quasienergies far from the branch cut, the topological characterization is not affected due to the localness of the spectral localizer. Nevertheless, standard matrix logarithm algorithms can struggle to correctly resolve angles when the spectrum of $\Pi(t_0 + T, t_0)$ lies near the branch cut. To get around this numerical issue we preshift the spectrum by $\Pi(t_0 + T, t_0) \to \Pi(t_0 + T, t_0)\exp(iET) = \exp[-i(H_F - EI)T]$. This has the effect of rotating the spectrum of the (unitary) monodromy matrix around the unit circle, centering the quasienergy value E on the positive real axis, opposite the branch cut. Without this shift, one will observe occasional incorrect readings of the local Chern number near $E = \pm\pi/T$ for the models considered in this work.

Overall, as the Floquet spectral localizer [Eq. (5)] can directly examine the topology in the system's bulk spectral gaps, our approach can distinguish between the trivial and the anomalous phases. Indeed, Figs. 1(c), 1(e), and 1(g) shows the energy-resolved local Chern numbers $C^{\text{L}}_{(x_0,y_0,E)}$ [Eq. (6)] throughout the quasienergy band, demonstrating in accordance to the other topological Floquet theory [25,28] that the anomalous Floquet phase is topological, despite having zero bulk Chern numbers. Notably, the Floquet spectral localizer is able to probe the local topology over local regions in a finite lattice, even in aperiodic lattices, as opposed to global indices [29,30] including the Bott index; a real-space version of the bulk-boundary correspondence can also be proved through the quadratic operator [50], even in the absence of bulk band gap: at locations where the local index changes, the quadratic operator guarantees nearby localized topological states, as shown in Appendix F. Due to the spectral shift mentioned above, in practice we set $E = 0$ in Eq. (5) since the spectral shift is performed prior to the logarithm in Eq. (4).

III. TOPOLOGICAL PROTECTION

The spectral localizer framework provides a rigorous treatment for predicting the system's topological protection. As the local topological markers constructed from the spectral localizer are all tied to its spectrum [37], the Clifford local gap, defined as

$$\mu^{\text{C}}_{(\boldsymbol{x},E)}(\boldsymbol{X}, H_{\text{F}}) = \min[|\text{spec}(L_{(\boldsymbol{x},E)}(\boldsymbol{X}, H_{\text{F}}))|], \tag{7}$$

gives a quantitative measure of the robustness of the topology; for a topological phase transition to take place, either as a result of system perturbations or changing the choice of $(\boldsymbol{x}, E)$, the local gap must close, $\mu^{\text{C}}_{(\boldsymbol{x},E)}(\boldsymbol{X}, H_{\text{F}}) = 0$. More precisely, we consider the perturbed Floquet system

$$i\frac{d\mathbf{u}_{\text{pert}}}{dt} = [H(t) + \delta H(t)]\mathbf{u}_{\text{pert}}(t), \tag{8}$$

where $\delta H(t)$ is a perturbation of the instantaneous Hamiltonian in Eq. (1) and is taken here to be a Hermitian and T-periodic matrix. Then the Floquet solution satisfies the evolution property $\mathbf{u}_{\text{pert}}(T) = \exp(-iTH_{\text{F,pert}})\mathbf{u}_{\text{pert}}(0)$, where $H_{\text{F,pert}}$ is the (Hermitian) perturbed Floquet Hamiltonian. Any change or perturbation in the Floquet Hamltonian $\delta H_{\text{F}} \equiv H_{\text{F,pert}} - H_{\text{F}}$ can be related to the local gap by

$$\left|\mu^{\text{C}}_{(\boldsymbol{x},E)}(\boldsymbol{X}, H_{\text{F,pert}}) - \mu^{\text{C}}_{(\boldsymbol{x},E)}(\boldsymbol{X}, H_{\text{F}})\right| \leqslant \|\delta H_{\text{F}}\|, \tag{9}$$

through an application of Weyl's spectral theorem [35,51], where $\|\cdot\|$ is the largest singular value of the matrix. As such, a topological transition cannot occur as long as

$$\|\delta H_{\text{F}}\| < \mu^{\text{C}}_{(\boldsymbol{x},E)}(\boldsymbol{X}, H_{\text{F}}), \tag{10}$$

as the perturbation is not strong enough to close the system's local gap so that the local topological marker can change its value.

While Eq. (9) yields a quantitative bound for the system's topological protection, this bound requires knowledge of the perturbed Floquet Hamiltonian, which may be challenging to determine in experimentally realizable systems. Instead, a more convenient formulation would work directly with the instantaneous perturbations $\delta H(t)$ in Eq. (8), since these instantaneous perturbations are a measurable quantity that can be readily modeled or bounded in experiments and realistic simulations. For example, given a perturbation with known harmonics (see Appendix D for more details and for other types of perturbation)

$$\delta H(t) = \delta_0 + \sum_{n=-N, n\neq 0}^{N} \delta_n e^{i\omega_n t}, \tag{11}$$

with ω_n being (integer) multiples of $\omega = 2\pi/T$, the difference in the Floquet Hamiltonians is bounded by $\rho(\delta H)$

$$\|\delta H_{\text{F}}\| \leqslant \rho(\delta H), \tag{12}$$

where

$$\rho(\delta H) = \|\overline{\delta H}\| + \sum_{n=-N, n\neq 0}^{N} \|\delta_n\|, \tag{13}$$

including the norm of the average

$$\|\overline{\delta H}\| = \left\| \frac{1}{T} \int_0^T dt\, \delta H(t) \right\|. \tag{14}$$

To avoid any issues coming from the chosen branch cut in the matrix log of the Floquet Hamiltonian, the bound is derived with no use of the matrix log but directly from the extended Floquet Hamiltonian defined over all the branches in the Fourier space, from which the bound is then deduced for the principal branch.

Thus, for a Floquet system in a given Chern phase at $(\boldsymbol{x}, E)$ indicated by $C^{\mathrm{L}}_{(\boldsymbol{x},E)}(\boldsymbol{X}, H_{\mathrm{F}})$,

$$\rho(\delta H) < \mu^{\mathrm{C}}_{(\boldsymbol{x},E)}(\boldsymbol{X}, H_{\mathrm{F}}) \Rightarrow C^{\mathrm{L}}_{(\boldsymbol{x},E)}(\boldsymbol{X}, H_{\mathrm{F,pert}}) = C^{\mathrm{L}}_{(\boldsymbol{x},E)}(\boldsymbol{X}, H_{\mathrm{F}}). \tag{15}$$

Notably, as opposed to earlier study [29,30], this inequality condition represents a predictive and quantitative measure of the topological robustness that is directly related to the driving protocol and experimentally accessible.

Intuitively, if the time average of the disorder and the spectral norm of the harmonics' perturbation are sufficiently small, then the topological phase at $C^{\mathrm{L}}_{(\boldsymbol{x},E)}(\boldsymbol{X}, H_{\mathrm{F}})$ is preserved in the presence of $\delta H(t)$.

Notice that Eq. (15) represents a sufficient condition for guaranteeing the persistence of a topological (or trivial) phase; however, in practice we find it is often more stringent than necessary for uncorrelated perturbations to preserve that phase.

The derived bound, Eq. (15), serves as a guide for identifying the degree of robustness at various space-energy locations, relating topological protection of Floquet systems to experimentally accessible parameters. To explore the topological protection in a toy model system from Fig. 1, we introduce on-site and coupling uncorrelated disorders drawn from a normal distribution with mean zero and standard deviation $\gamma\Delta$ and γJ, respectively, while keeping $\delta H(t)$ Hermitian (see Appendix E). In waveguide systems, the former represents a perturbation of self-interaction Δ, i.e., a variation in the local refractive index. The latter type of disorder can be used to model perturbations to the coupling coefficient J, e.g., inconsistent coupling strengths between pairs of waveguides. As the strength of the disorder is increased, quantified by $\rho(\delta H)$ [Eq. (12)], the topologically nontrivial region degrades along the boundaries and ultimately ruptures into smaller domains, as shown in Figs. 2 and 3. When the disorder strength is smaller than the local gap of the unperturbed system $\mu_0^{\mathrm{clean}} \equiv \mu^{\mathrm{C}}_{(\boldsymbol{x}_0,E_0)}(\boldsymbol{X}, H_{\mathrm{F}})$, namely $\rho/\mu_0^{\mathrm{clean}} < 1$, the topology of the system remains unchanged, thereby demonstrating the validity of derived bound in Eq. (15). Nevertheless, the persistence of the nontrivial topology at larger disorder strengths, $\rho/\mu_0^{\mathrm{clean}} > 1$, illustrates that the inequality in Eq. (15) serves as a sufficient, but not necessary, condition for preserving the topology. Altogether, we have derived a quantitative measure of topological robustness that can be directly related to perturbations of the system during the driving protocol and, as such, larger local gaps in the clean system yield stronger topological robustness, as shown in Appendix B with the nontrivial Floquet anomalous topology at the π-gap.

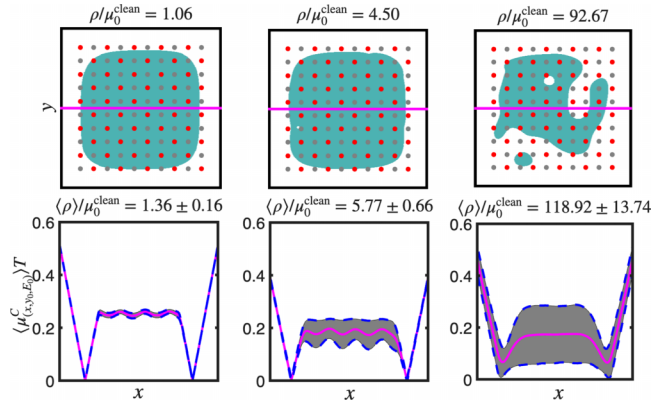

FIG. 2. (Top row) One realization of the local 0-gap Chern number $C^{L}_{(\boldsymbol{x},E_0)}$ $(E_0 = 0)$ (6) as the strength of on-site disorder is increased, left to right, in the anomalous insulator. The magenta line indicates the location of y_0. (Bottom row) Ensemble averaged local gap width (7) at y_0, with $\kappa = 0.5/(Ta)$. Error bars denoting one standard deviation are included.

IV. CONCLUSION

In conclusion, we have developed a general framework, based on the spectral localizer, to classify the local topology in Floquet systems directly and solely from the system's Floquet Hamiltonian and quantify their topological protection. Although the topology is expressed from a stroboscopic point of view with the Floquet Hamiltonian, we have derived a relation between topological protection and perturbation of the instantaneous Hamiltonian as in the static case and show that nontrivial topology survives as long as both the time average of the instantaneous perturbation and the spectral norm of the harmonics' perturbation are smaller than the local gap. In essence, this provides a predictive and quantitative measure of the topological robustness before which a topological transition can arise due to disorder.

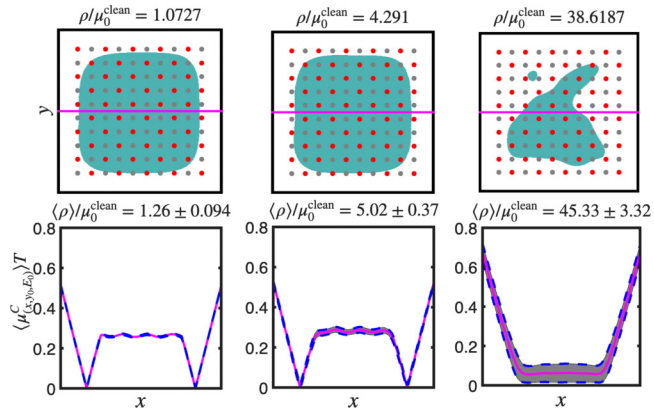

FIG. 3. (Top row) One realization of the local 0-gap Chern number $C^{L}_{(\boldsymbol{x},E_0)}$ $(E_0 = 0)$ (6) as the strength of coupling disorder is increased, left to right, in the anomalous insulator. The magenta line indicates the location of y_0. (Bottom row) Ensemble averaged local gap width (7) at y_0, $\kappa = 0.5/(Ta)$. Error bars denoting one standard deviation are included.

Furthermore, as the spectral localizer for Floquet systems utilized the Floquet Hamiltonian, derived from the monodromy matrix, rather than the Hamiltonian of the governing equations, the spectral localizer formulation is equation-free and provides a data-driven approach to probe the topology [52]. Notably, given a lattice, the monodromy matrix can be constructed as in Eq. (2) by individually exciting each site of the lattice and then measuring the phases and amplitudes at each site after one period, which is an experimental protocol that should readily be applicable in a variety of Floquet systems [9,53,54]. In other words, the spectral localizer framework provides a system agnostic method to experimentally verify the topology of a Floquet system by computing the local index, derived from the monodromy matrix, and does not rely on a specific system's property, as opposed to more specialized approaches [30,55,56] based on response theory specific to particular systems. Looking forward, we anticipate our operator-based framework should be useful for diagnosing the topology and its topological robustness from a range of physical photonic Floquet systems such as waveguiding or pump-driven systems [14,16,17,19–23].

Note added. Recently, we became aware of a similar proposal posted on a server [57] that also develops a theory of Floquet topological systems based on the spectral localizer.

ACKNOWLEDGMENTS

S.W. acknowledges support from the Laboratory Directed Research and Development program at Sandia National Laboratories. A.C. acknowledges support from the U.S. Department of Energy, Office of Basic Energy Sciences, Division of Materials Sciences and Engineering. J.T.C. acknowledges support from the Air Force Office of Scientific Research under Grant No. FA9550-23-1-0105. This work was performed, in part, at the Center for Integrated Nanotechnologies, an Office of Science User Facility operated for the U.S. Department of Energy (DOE) Office of Science. Sandia National Laboratories is a multimission laboratory managed and operated by National Technology & Engineering Solutions of Sandia, LLC, a wholly owned subsidiary of Honeywell International, Inc., for the U.S. DOE's National Nuclear Security Administration under Contract No. DE-NA-0003525.

The views expressed in the article do not necessarily represent the views of the U.S. DOE or the United States Government.

APPENDIX A: OUTPUT OF THE SPECTRAL LOCALIZER

In this section the output of the Floquet localizer is shown and discussed. These results were generated for the Hamiltonian shown in Fig. 1. Here, we consider a 10×10 square lattice with the five-stage driving protocol described in Fig. 1, with coupling strength J and detuning mass term $\mp\Delta$ applied to the a and b sublattice sites, respectively, and along with corresponding quasienergy bands.

The first case is the topological transition in the π-gap that occurs around $JT \approx 1.1\pi$. The results of the Floquet localizer are summarized in Fig. 4. Above this critical hopping amplitude, the local Chern index is $C^L_{(\boldsymbol{x},E_\pi)} = 1$ in the π-gap. To compute this, we choose quasienergy $E_\pi = \pi/T$ and scan

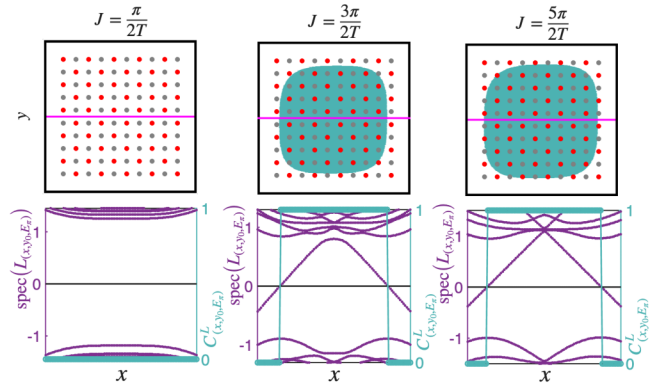

FIG. 4. Topological transition in the π-gap ($E_\pi = \pi/T$) as the hopping amplitude increases. (Top row) The value of $C^L_{(\boldsymbol{x},E_\pi)}$ relative to the lattice; white (teal) denotes 0 (1). The magenta line indicates the probing locations of the bottom row. (Bottom row) Floquet localizer spectrum and local index at y_0, $\kappa = 0.5/(Ta)$.

spatial points both inside and outside the lattice. The localizer indicates a nontrivial topology fills most of the interior lattice region. The bottom row of Fig. 4 highlights the change in topology coincides with a change in the signature, defined in Eq. (6).

As a practical note, in the π-gap we find it useful to rotate the monodromy matrix by $\Pi(T,0) \to \Pi(T,0)\exp(iETI)$, where I denotes the identity matrix, to compute the quasienergy E for the evolution operator defined in Eq. (4). Doing this at this stage amounts to performing the spectral shift in the diagonal of Eq. (5) before the logarithm, rather than after.

The second topological transition occurs at approximately $JT \approx 2\pi$ in the 0-gap. Typical Floquet localizer results for this gap are shown in Fig. 5. Above this transition point, the local Chern number is $C^L_{(\boldsymbol{x},E_0)} = 1$ ($E_0 = 0$) in a region that fills most of the square lattice. As highlighted in the main article, the local Chern index is able to identify topologically nontrivial states where the normal Chern number does not.

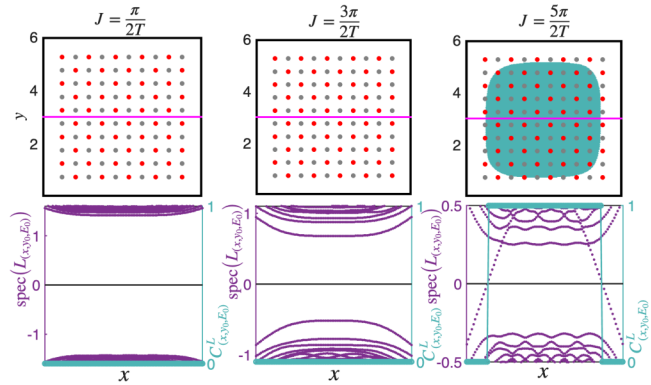

FIG. 5. Topological transition in the 0-gap ($E_0 = 0$) as the hopping amplitude increases. (Top row) The value of $C^L_{(\boldsymbol{x},E_0)}$ relative to lattice; white (teal) denotes 0 (1). The magenta line indicates the probing locations of the bottom row. (Bottom row) Floquet localizer spectrum and local index at y_0, $\kappa = 0.5/(Ta)$.

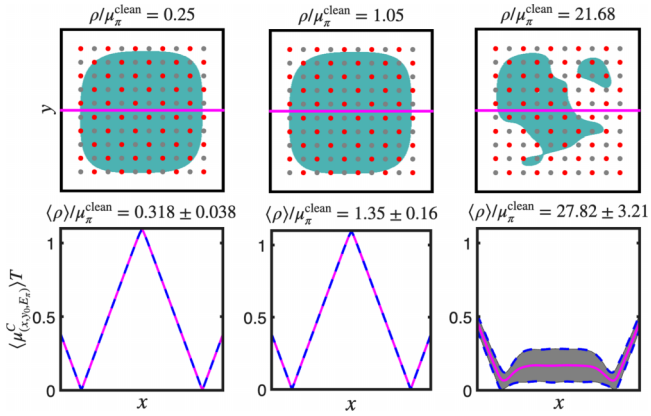

FIG. 6. (Top row) One realization of the local π-gap Chern number $C^L_{(\boldsymbol{x},E_\pi)}$ ($E_\pi = \pi/T$) (6) as the strength of on-site disorder is increased, left to right, in the anomalous state. The magenta line indicates the location of y_0. (Bottom row) Ensemble averaged local gap width (7) at y_0, $\kappa = 0.5/(Ta)$. Error bars denoting one standard deviation are included.

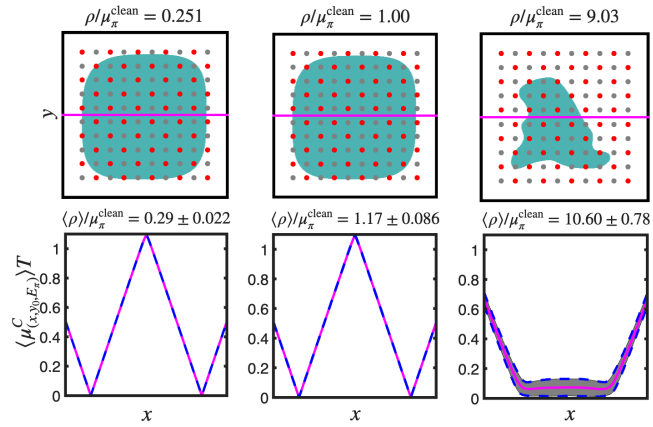

FIG. 7. (Top row) One realization of the local π-gap Chern number $C^L_{(\boldsymbol{x},E_\pi)}$ ($E_\pi = \pi/T$) (6) as the strength of coupling disorder is increased, left to right, in the anomalous state. The magenta line indicates the location of y_0. (Bottom row) Ensemble averaged local gap width (7) at y_0, $\kappa = 0.5/(Ta)$. Error bars denoting one standard deviation are included.

Examining the local gaps in Figs. 4 and 5, we can say that the perimeter (interior) of the lattice region is the most (least) susceptible to a topological transition. The reason is that the local gap [defined in Eq. (7)] is smallest (largest) near the edge (bulk) of the lattice. Moreover, the π-gap should be more resilient to disorder than the 0-gap since $\mu^C_{(\boldsymbol{x},E_\pi)}$ is larger than $\mu^C_{(\boldsymbol{x},E_0)}$ in the bulk region. For the anomalous system at the central lattice point $\boldsymbol{x}_0$, $\mu^C_{(\boldsymbol{x}_0,E_\pi)} \approx 4\mu^C_{(\boldsymbol{x}_0,E_0)}$ and so, relative to the 0-gap modes, π-gap states are sustained under disorder that is about four times as strong. Simulations confirm these intuitions.

APPENDIX B: TOPOLOGICAL PROTECTION FOR π-GAP STATES

This section complements the study of topology in the presence of disorder discussed in the main article. Here, the disorder of the π-gap, rather than the 0-gap, is examined.

The effect of disorder on π-gap states is highlighted in Figs. 6 and 7 for on-site and coupling disorder, respectively. In each case, the disorder parameter ρ relative to the gap width $\mu_\pi^{\text{clean}} \equiv \mu^C_{(\boldsymbol{x}_0,E_\pi)}(H_{\text{F}})$ is given. Note that the disorder used in these figures is identical to that used in Figs. 2 and 3, respectively. The overall trend is similar: as the strength of disorder increases, the topological state deteriorates.

As mentioned before, the π-gap is a wider and more robust gap than the 0-gap for these parameters. As a result, these cases tend to be more contiguous and intact in comparison to their 0-gap counterpart. This can be attributed to the larger $\mu^C_{(\boldsymbol{x},E)}$ values in the lattice.

The values of disorder chosen here highlight the theorem in Eq. (15), where topological protection is guaranteed when $\rho/\mu^{\text{clean}}_{(\boldsymbol{x},E)} < 1$. Hence, for detuning disorder up to 17% of Δ (see Fig. 6, middle column), the π-gap topological state is preserved. Recall the 0-gap state could be guaranteed up to approximately 4% of Δ (see Fig. 2, left column). On the other hand, the states in the π-gap are preserved for coupling perturbations up to 2% of J (see Fig. 7, middle column) while the 0-gap is stable for approximately 0.5% of J (see Fig. 3, left column).

The last columns of Figs. 2, 3, 6, and 7 highlight that, for sufficiently strong disorder $\rho/\mu^{\text{clean}}_{(\boldsymbol{x},E)} \gg 1$, the topological state will break up.

APPENDIX C: SELECTION OF HYPERPARAMETER κ

The value of κ in the Floquet localizer defined in Eq. (5) should be chosen to balance the quasienergy and spatial scales. As discussed in [33], an appropriate value is $\kappa \approx E_{\text{gap}}/L$, where E_{gap} is the spectral gap width (units of inverse time) and L is the total length of the lattice (units of length). Hence, for Floquet problems, this hyperparameter has units of frequency per unit length.

For the cases shown in Fig. 1, the gap widths are approximately $0.2(\pi/T) \leqslant E_{\text{gap},0} \leqslant 1(\pi/T)$ and $0.6(\pi/T) \leqslant E_{\text{gap},\pi} \leqslant 1.5(\pi/T)$ for the zero and π-gaps, respectively. For our lattice, the length scale is $L = 4.5a$, which suggests a common value of $\kappa = 0.5/(Ta)$, for all cases, with $T = 1$, $a = 1$; this was the value of κ used to generate all figures in this paper.

To confirm the appropriateness of this choice of κ, the local Chern number and gap width for the Floquet Hamiltonian is computed at different values of κ. The localizer output for κ between $0.01/(Ta)$ and $2/(Ta)$ is shown in Fig. 8. The spatial sample point corresponds to the center of our finite square lattice $(x_0, y_0) = (3, 3)$ and the quasienergy value is at the center of the zero or π-gap, respectively (see Fig. 1). For each case considered, the choice of $\kappa = 0.5/(Ta)$ corresponds to the appropriate value of the local spectral index.

APPENDIX D: BOUNDING δH_{F}

In this section we derive the bound in Eq. (12) of the main article.

Recall the definition of the Floquet Hamiltonian, given in Eq. (4) of the main text, is computed via the matrix loga-

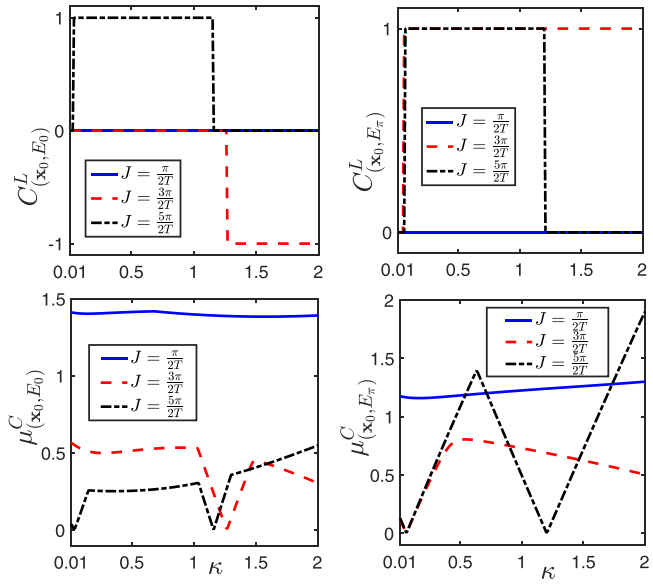

FIG. 8. (Top row) Local Chern index (6) and (bottom row) local gap width (7) as a function of parameter κ [in units of $1/(Ta)$] for the Floquet Hamiltonian using $\Delta = \frac{\pi}{2T}$. The sample point $\boldsymbol{x}_0$ is at the center of the lattice.

rithm of the monodromy matrix. It is well known that the log function is a multivalued function in the complex plane and a branch cut is introduced to make it single valued. Here we take the principal branch cut, located along the negative real axis, between zero and $-\infty$. In the context of Eq. (8) of the main article, as we move from the clean [$\delta H(t) = 0$] to disordered problem, the Floquet Hamiltonian changes from $H_{\rm F}$ to $H_{\rm F,pert}$. As such, to derive a bound on the perturbation of the Floquet Hamiltonian, we use the extended Floquet Hamiltonian defined in the entire Floquet space, contrary to a single Floquet zone, thus avoiding issues with eigenvalues crossing branch cuts.

1. Extended Floquet Hamiltonian $\mathbb{H}_{\rm F}$

Each column of the monodromy matrix satisfies the governing equation [Eq. (1)] of the main article,

$$i\frac{d\mathbf{u}}{dt} = H(t)\mathbf{u}. \tag{D1}$$

Due to the periodicity in time, with period T, the solutions have the Floquet-Fourier form

$$\mathbf{u}(t) = e^{-iEt}\sum_{m=-\infty}^{\infty}\widehat{\boldsymbol{u}}_m\, e^{im\omega t}, \tag{D2}$$

for the temporal frequency $\omega = 2\pi/T$. The time-dependent and periodic Hamiltonian matrix is also expanded in a Fourier series,

$$H(t) = \sum_{m=-\infty}^{\infty}\widehat{H}_m e^{im\omega t}, \tag{D3}$$

with the Fourier coefficients given by

$$\widehat{H}_m = \frac{1}{T}\int_0^T dt\, e^{-im\omega t}H(t). \tag{D4}$$

Substituting expansions Eq. (D2)–(D4) into the governing equation (D1), one finds

$$\sum_{m'=-\infty}^{\infty}\left[\frac{1}{T}\int_0^T dt\, e^{-im'\omega t}H(t)\right]\widehat{\mathbf{u}}_{m-m'} - m\omega\widehat{\mathbf{u}}_m = E\widehat{\mathbf{u}}_m \tag{D5}$$

for $m = -\infty, \ldots, \infty$. Notice that the left hand side is a Fourier version of the Floquet Hamiltonian, referred to here as the extended Floquet Hamiltonian $\mathbb{H}_{\rm F}$, for which the eigenvalue problem in Eq. (D5) is then expressed as

$$\mathbb{H}_{\rm F}\widehat{\boldsymbol{\psi}} = E\widehat{\boldsymbol{\psi}}. \tag{D6}$$

For example, truncating to $m = -2, \ldots, 2$ and $m' = -2, \ldots, 2$, the extended Floquet Hamiltonian is given by

$$\mathbb{H}_{\rm F} = \begin{pmatrix} \widehat{H}_0 - 2\omega I & \widehat{H}_{-1} & \widehat{H}_{-2} & 0 & 0 \\ \widehat{H}_1 & \widehat{H}_0 - \omega I & \widehat{H}_{-1} & \widehat{H}_{-2} & 0 \\ \widehat{H}_2 & \widehat{H}_1 & \widehat{H}_0 & \widehat{H}_{-1} & \widehat{H}_{-2} \\ 0 & \widehat{H}_2 & \widehat{H}_1 & \widehat{H}_0 + \omega I & \widehat{H}_{-1} \\ 0 & 0 & \widehat{H}_2 & \widehat{H}_1 & \widehat{H}_0 + 2\omega I \end{pmatrix}, \tag{D7}$$

with $\widehat{\boldsymbol{\psi}} = [\widehat{\mathbf{u}}_{-2}, \widehat{\mathbf{u}}_{-1}, \widehat{\mathbf{u}}_0, \widehat{\mathbf{u}}_1, \widehat{\mathbf{u}}_2]^T$.

One important difference between Eq. (D6) and Eq. (4) of the main article is that Eq. (D6) does not involve a logarithm. As a result, Eq. (D6) and its spectrum are not restricted to the principal Floquet zone; it is an *extended* Floquet Hamiltonian. The spectrum of Eq. (D6) is infinite, but agrees with the quasienergies of Eq. (4), obtained from the matrix log, in the region $[-\pi/T, \pi/T)$. In particular, the spectrum of the Floquet Hamiltonian $H_{\rm F}$ obtained from the matrix log can be considered as the spectrum of the extended Floquet Hamiltonian $\mathbb{H}_{\rm F}$ when truncated to a single Floquet zone, say $m = 0$ with quasienergies within $[-\pi/T, \pi/T)$. As such, defining the projection operator $\mathcal{P}$ that removes all eigenmodes whose corresponding eigenvalues do *not* reside in the interval $[-\pi/T, \pi/T)$, we have

$$\|H_{\rm F}\| = \|\mathcal{P}^\dagger\mathbb{H}_{\rm F}\mathcal{P}\|. \tag{D8}$$

2. Perturbation $\delta\mathbb{H}_{\rm F}$ in the extended Floquet Hamiltonian

An additional observation is that Eq. (D6) depends directly on the time-dependent Hamiltonian. Hence a Floquet Hamiltonian defined similar to Eq. (D6) can be used for the perturbed problem in Eq. (8) of the main article. Then we can write down a perturbed eigenvalue problem

$$\mathbb{H}_{\rm F,pert}\widehat{\boldsymbol{\psi}}_{\rm pert} = E_{\rm pert}\widehat{\boldsymbol{\psi}}_{\rm pert}, \tag{D9}$$

with the only difference being that $\mathbb{H}_{\rm F,pert}$ replaces $H(t)$ with $H(t) + \delta H(t)$. In other words,

$$\sum_{m'=-\infty}^{\infty}\left[\frac{1}{T}\int_0^T dt\, e^{-im'\omega t}\big(H(t) + \delta H(t)\big)\right]\widehat{\mathbf{u}}_{m-m'} - m\omega\widehat{\mathbf{u}}_m = E_{\rm pert}\widehat{\mathbf{u}}_m \tag{D10}$$

for $m = -\infty, \ldots, \infty$. If we write $\mathbb{H}_{\rm F,pert}$ as

$$\mathbb{H}_{\rm F,pert} = \mathbb{H}_{\rm F} + \delta\mathbb{H}_{\rm F}, \tag{D11}$$

then the perturbation matrix to the clean extended Floquet Hamiltonian $\mathbb{H}_{\mathrm{F}}$, denoted $\delta\mathbb{H}_{\mathrm{F}}$, can be defined via the following equation:

$$\sum_{m'=-\infty}^{\infty}\left[\frac{1}{T}\int_0^T dt\, e^{-im'\omega t}\delta H(t)\right]\widehat{\mathbf{u}}_{m-m'} = \delta E\widehat{\mathbf{u}}_m. \tag{D12}$$

Analogous to Eq. (D7) (without the $m\omega I$ terms), $\delta\mathbb{H}_{\mathrm{F}}$ can be written as the sum of Kronecker products

$$\delta\mathbb{H}_{\mathrm{F}} = \sum_{n=-\infty}^{\infty}\delta\widehat{H}_n\otimes A_{-n}, \tag{D13}$$

with

$$\delta\widehat{H}_n = \frac{1}{T}\int_0^T dt\, e^{-in\omega t}\delta H(t) \tag{D14}$$

and A_n being the matrices defined with 1's on the nth diagonals and zero elsewhere, e.g., $A_0 = I$,

$$A_{-1} = \begin{pmatrix} \ddots & & & & & & \\ \ddots & 0 & & & & & \\ & 1 & 0 & & & & \\ & & 1 & 0 & & & \\ & & & 1 & 0 & & \\ & & & & \ddots & \ddots \end{pmatrix},$$

$$A_1 = \begin{pmatrix} \ddots & \ddots & & & & & \\ & 0 & 1 & & & & \\ & & 0 & 1 & & & \\ & & & 0 & 1 & & \\ & & & & 0 & \ddots & \\ & & & & & \ddots \end{pmatrix}.$$

Notably, the spectral norm of the perturbation $\delta\mathbb{H}_{\mathrm{F}}$ in the extended Floquet zone is an upper bound of the spectral norm of the perturbation δH_{F} in the $m = 0$ Floquet zone:

$$\|\delta H_{\mathrm{F}}\| = \|\mathcal{P}^{\dagger}\delta\mathbb{H}_{\mathrm{F}}\mathcal{P}\| \leqslant \|\delta\mathbb{H}_{\mathrm{F}}\|. \tag{D15}$$

What remains is therefore to find an upper bound of $\delta\mathbb{H}_{\mathrm{F}}$, denoted $\rho(\delta H)$, i.e.,

$$\|\delta\mathbb{H}_{\mathrm{F}}\| \leqslant \rho(\delta H), \tag{D16}$$

for which the starting point is given by

$$\begin{aligned}\|\delta\mathbb{H}_{\mathrm{F}}\| &= \left\|\sum_{n=-\infty}^{\infty}\delta\widehat{H}_n\otimes A_{-n}\right\| \\ &\leqslant \sum_{n=-\infty}^{\infty}\|\delta\widehat{H}_n\otimes A_{-n}\| \\ &= \sum_{n=-\infty}^{\infty}\|\delta\widehat{H}_n\|\|A_{-n}\| \\ &\leqslant \|\delta\widehat{H}_0\| + \sum_{n=1}^{\infty}\|\delta\widehat{H}_{-n}\| + \sum_{n=1}^{\infty}\|\delta\widehat{H}_n\|,\end{aligned} \tag{D17}$$

with

$$\|\delta\widehat{H}_0\| = \left\|\frac{1}{T}\int_0^T dt\,\delta H(t)\right\| = \|\overline{\delta H}\| \tag{D18}$$

and where we have used the triangle inequality, $\|A\otimes B\| = \|A\|\|B\|$ and $\|A_n\| = 1$. In practice, we consider a truncation of A_n that is arbitrarily large but finite.

Altogether, an upper bound of δH_{F} is therefore given by

$$\|\delta H_{\mathrm{F}}\| \leqslant \rho(\delta H). \tag{D19}$$

This inequality is significant as it relates the perturbation of a Floquet Hamiltonian to the perturbation of a time-dependent Hamiltonian. The explicit detail of the upper bound $\rho(\delta H)$ will be derived in the next subsection and will be the main result of this section to track the robustness of the topology.

3. Upper bound on the perturbation in the extended Floquet Hamiltonian $\delta\mathbb{H}_{\mathrm{F}}$

In this subsection, we derive the upper bound $\rho(\delta H)$ for particular perturbation cases, which corresponds to most physically realizable Floquet systems.

a. Perturbation with known harmonics driving

We first begin with the case where the perturbation has known harmonic drivings ($\delta_n e^{-i\omega_n t}$). As such, the perturbation is written in terms of a finite sum of harmonics

$$\delta H(t) = \delta_0 + \sum_{n=-N,n\neq 0}^{N}\delta_n e^{i\omega_n t}, \tag{D20}$$

with ω_n being (integer) multiples of $\omega = 2\pi/T$, δ_0 and δ_n are constant matrices, and the upper bound is thus given by

$$\rho(\delta H) = \|\overline{\delta H}\| + \sum_{n=-N,n\neq 0}^{N}\|\delta_n\|. \tag{D21}$$

b. Perturbation with analytic behavior

Here, we consider a more general case where the perturbation does not have a known harmonic driving. Physically, we assume that all perturbations are infinitely smooth functions in time (with all derivatives being continuous) and that the perturbation has a converging Taylor series. Now, consider complexifying $\delta H(t)$ in terms of the complex variable $z = t - i\eta$. Assume $\delta H(z)$ is analytic in a strip $-\eta < \mathrm{Im}(z) < \eta$, for $\eta > 0$. Using Cauchy's theorem and the periodic boundary conditions, the Fourier coefficient $\delta\widehat{H}_n$ can be written as

$$\begin{aligned}\delta\widehat{H}_n &= \frac{1}{T}\int_0^T dt\, e^{-in\omega t}\delta H(t) \\ &= \frac{1}{T}\int_{-i\eta}^{T-i\eta} dz\, e^{-in\omega z}\delta H(z)\end{aligned} \tag{D22}$$

and

$$\begin{aligned}\|\delta\widehat{H}_n\| &\leqslant \frac{1}{T}\int_{-i\eta}^{T-i\eta} dz\|e^{-in\omega z}\delta H(z)\| \\ &\leqslant \frac{1}{T}e^{-n\omega\eta}C\int_{-i\eta}^{T-i\eta} dz \\ &= C\, e^{-n\omega\eta},\end{aligned} \tag{D23}$$

where $C = \max\{\|\delta H(z)\|, \mathrm{Re}(z)\in[0,T], \mathrm{Im}(z) = -\eta\}$ is the maximum of the norm of the perturbation on the line $z = -i\eta$ in the lower half complex plane. A symmetric argument for

$n < 0$ can be formulated in the upper half plane, adding a factor of 2 to the bound. Altogether,

$$\|\delta\mathbb{H}_{\mathrm{F}}\| \leqslant \|\overline{\delta H}\| + 2C\sum_{n=1}^{\infty} e^{-n\omega\eta} = \|\overline{\delta H}\| + \frac{2C}{e^{\eta\omega}-1} \tag{D24}$$

and the upper bound is expressed as

$$\rho(\delta H) = \|\overline{\delta H}\| + \frac{2C}{e^{\eta\omega}-1}. \tag{D25}$$

c. Perturbation with piecewise differentiable behavior

Here, we exclude any cases that are pathological which are thus reasonably nonphysical and assume that the perturbations exhibit "good" enough behavior. We define $H^{q}_{\mathrm{per}}([0,T])$ to be a Sobolev space consisting of matrix functions with periodic boundary conditions and q square integrable derivatives. We define $C^{q}_{\mathrm{per}}([0,T])$ the space of periodic matrix functions with q continuous derivatives. We assume that $\delta H(t) \in H^{k}_{\mathrm{per}}([0,T]) \cap C^{k-2}_{\mathrm{per}}([0,T])$, for $k \geqslant 2$, meaning that the perturbation $\delta H(t)$ is periodic and the derivatives $q = 0,\ldots,k-2$ are continuous and square integrable, and the k-th derivative is square integrable.

We consider a $(k-1)$th derivative $\delta H^{(k-1)}(t)$ which is piecewise smooth at finitely many points and has bounded variation. Then the time interval is subdivided into N subintervals by $\delta H^{(k-1)}(t) = \delta H^{(k-1)}_{i+1}(t)$, $t \in (T_i, T_{i+1})$, $i = 0,\ldots,N-1$, $T_0 = 0$, $T_N = T$, and $T_{-1} = T_{N-1}$. Next, using integration by parts, the Fourier coefficient $\delta\widehat{H}_n$ for $n \neq 0$ can be expressed as

$$\delta\widehat{H}_n = \frac{1}{T}\frac{1}{(-in\omega)^k}\sum_{i=1}^{N} e^{-in\omega T_i}\left(\delta H^{(k-1)}_{i}(T_i) - \delta H^{(k-1)}_{i+1}(T_i)\right) + \frac{1}{T}\frac{1}{(-in\omega)^k}\int_0^T dt\, e^{-in\omega t}\delta H^{(k)}(t). \tag{D26}$$

Note that, due to periodicity, $\delta H^{(q)}_{N+1} = \delta H^{(q)}_{1}$ for any $q \geqslant 0$. Here, $\delta H^{(q)}_{i+1}(T_i) = \lim_{t\to T_i^+}\delta H^{(q)}_{i+1}(t)$ and $\delta H^{(q)}_{i}(T_i) = \lim_{t\to T_i^-}\delta H^{(q)}_{i}(t)$ denote right and left limits, respectively. In Eq. (D26), the first term accounts for a jump in perturbation where a discontinuity exists and the left and right limits do not match. An upper bound of the nonzero Fourier coefficients can be found as

$$\|\delta\widehat{H}_n\| \leqslant \frac{1}{T}\frac{1}{(|n|\omega)^k}\sum_{i=1}^{N}\left\|\delta H^{(k-1)}_{i}(T_i) - \delta H^{(k-1)}_{i+1}(T_i)\right\| + \frac{1}{(|n|\omega)^k}\|\overline{\delta H^{(k)}}\|, \tag{D27}$$

where

$$\|\overline{\delta H^{(k)}}\| = \left\|\frac{1}{T}\int_0^T dt\,\delta H^{(k)}(t)\right\| \tag{D28}$$

is the time average of the kth time derivative of the perturbation $\delta H^{(k)}(t)$.

Plugging Eq. (D27) into Eq. (D17), the upper bound of $\delta\mathbb{H}_{\mathrm{F}}$ now reads

$$\|\delta\mathbb{H}_{\mathrm{F}}\| \leqslant \|\overline{\delta H}\| + 2\left(\sum_{n=1}^{\infty}\frac{1}{n^k}\right)\times\frac{1}{\omega^k}\frac{1}{T}\sum_{i=1}^{N}\left\|\delta H^{(k-1)}_{i}(T_i) - \delta H^{(k-1)}_{i+1}(T_i)\right\| + \left(\sum_{n=1}^{\infty}\frac{1}{n^k}\right)\frac{2}{\omega^k}\|\overline{\delta H^{(k)}}\|. \tag{D29}$$

The second and third terms converge provided $k > 1$. That is, provided $\delta H^{(1)}(t)$ is an integrable function (jumps are finite valued), the bound in (D29) converges. If $k \leqslant 1$, then the series does not converge. An example of a problematic function is a piecewise constant perturbation where $k = 1$.

However, in physically relevant systems, jumps in the perturbation can always be assumed to be smoothed out in experiment and therefore continuous. As such, jumps between $\delta H_i(T_i)$ and $\delta H_{i+1}(T_i)$ can be regularized by interpolating the jump, for example, with a linear spline within the interval $[T_i - h, T_i + h]$, for $0 < h \ll T$,

$$\delta H_{i,i+1}(t) = \delta H_i(T_i) + \frac{\delta H_{i+1}(T_i) - \delta H_i(T_i)}{2h}(t - T_i + h), \tag{D30}$$

where

$$\delta H_{i,i+1}(T_i - h) = \delta H_i(T_i), \tag{D31}$$

$$\delta H_{i,i+1}(T_i + h) = \delta H_{i+1}(T_i), \tag{D32}$$

$$\delta H_{i,i+1}(T_i) = \frac{\delta H_i(T_i) + \delta H_{i+1}(T_i)}{2}. \tag{D33}$$

Notably, this is enough for $k = 2$ in Eq. (D29) with,

$$\delta H^{(1)}_{i,i+1}(t) = \frac{\delta H_{i+1}(T_i) - \delta H_i(T_i)}{2h}. \tag{D34}$$

Altogether, the local regularized Hamiltonian perturbation is

$$\delta H(t) = \begin{cases} \delta H_i(t), & t \in (T_{i-1}+h, T_i - h), \\ \delta H_{i,i+1}(t), & t \in [T_i - h, T_i + h], \\ \delta H_{i+1}(t), & t \in (T_i + h, T_{i+1} - h), \end{cases} \tag{D35}$$

denoting a continuous function with a now-removed jump at T_i. Note that, here, the specific details of the interpolation are not important, except removing the diverging terms, and the interpolation can be chosen to be as smooth as possible to avoid contributing to additional terms in the upper bound. After regularizing Eq. (D29), the bound in Eq. (D29) is valid for $k = 2$.

While utilizing the highest k possible might be preferable, as tighter upper bounds are obtained with increased k in the $1/n^k$ terms, only a closed form of the series is known so far for $k = 2p$ even, involving the Bernoulli numbers B_{2p}

$$\zeta(2p) = \sum_{n=1}^{\infty}\frac{1}{n^{2p}} = (-1)^{p+1}\frac{B_{2p}(2\pi)^{2p}}{2(2p)!}, \tag{D36}$$

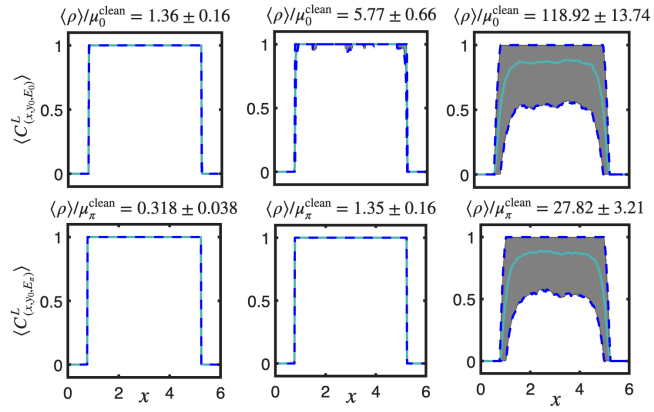

FIG. 9. Ensemble average of the local Chern index (6) in the (top row) 0-gap and (bottom row) π-gap for the anomalous Floquet Hamiltonian with on-site disorder. To compute these averages, 1000 realizations were taken. The values taken are $(y_0, \kappa) = [3, 0.5/(Ta)]$ and (top) $E_0 = 0$, (bottom) $E_\pi = \pi/T$. The top (bottom) row corresponds to the case shown in Fig. 2 (6).

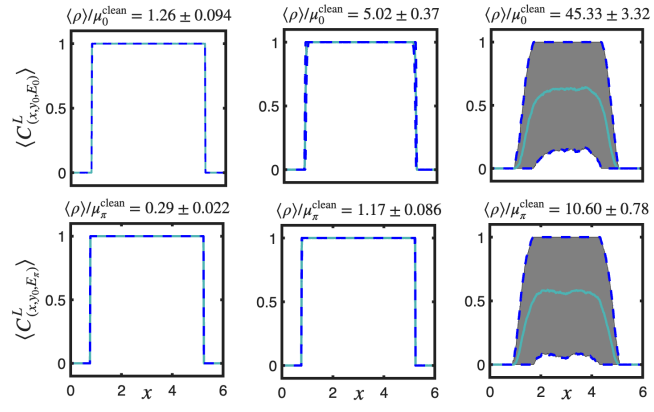

FIG. 10. Ensemble average of the local Chern index (6) in the (top row) 0-gap and (bottom row) π-gap for the anomalous Floquet Hamiltonian with coupling disorder. To compute these averages, 1000 realizations were taken. The values taken are $(y_0, \kappa) = [3, 0.5/(Ta)]$ and (top) $E_0 = 0$, (bottom) $E_\pi = \pi/T$. The top (bottom) row corresponds to the case shown in Fig. 3 (7).

yielding $\zeta(2) = \pi^2/6 \approx 1.65$, $\zeta(4) = \pi^4/90 \approx 1.1$, etc. As such, $k = 2$ is sufficient for an upper bound, meaning

$$\rho(\delta H) = \|\overline{\delta H}\| + \frac{T}{12}\sum_{i=1}^{N}\left\|\delta H_i^{(1)}(T_i) - \delta H_{i+1}^{(1)}(T_i)\right\| + \frac{T^2}{12}\|\overline{\delta H^{(2)}}\|. \tag{D37}$$

APPENDIX E: DISORDERED HAMILTONIAN

In the main article, we considered topology in the presence of uncorrelated disorder. For each case, random normally distributed real numbers with mean zero and variable standard deviation were used.

We exemplify perturbation with known harmonics, which is typical for Floquet systems using photonic waveguides. As such, the perturbation reads

$$\delta H(t) = \tfrac{3}{2}\delta_0 + \tfrac{1}{2}\delta_{10}\cos(10\omega t) \tag{E1}$$

and the relevant upper bound is given by

$$\rho(\delta H) = \tfrac{3}{2}\|\delta_0\| + \tfrac{1}{2}\|\delta_{10}\|. \tag{E2}$$

Two types of disorder for $\delta H(t)$ were considered: on-site and coupling, meaning the entries of the matrices δ_0 and δ_{10} are populated accordingly, as explained in the following paragraphs.

To create on-site disorder, random numbers of the form r_j are added to each site along the diagonal of δ_0 and δ_{10}. These random values are chosen with mean zero, $\langle r_j\rangle = 0$, and standard deviation $\sqrt{\langle r_j^2\rangle} = \gamma\Delta$, scaled relative to the detuning mass term Δ. The value of γ is the same for both δ_0 and δ_{10}. The unperturbed $[\delta H(t) = 0]$ case corresponds to $\gamma = 0$. The three columns in Figs. 2, 6, and 9 correspond to $\gamma = 0.04,\ 0.17$, and 3.5, respectively. Relatively large values of γ are taken since the system is quite robust to on-site disorder.

A few typical average local Chern numbers are shown in Fig. 9. In each figure, the top and bottom error bars, denoted by blue dashed lines, are defined by

$$\min\left\{1, \langle C^L_{(\boldsymbol{x},E)}\rangle + \sqrt{\langle\left(C^L_{(\boldsymbol{x},E)} - \langle C^L_{(\boldsymbol{x},E)}\rangle\right)^2\rangle}\right\}, \tag{E3}$$

$$\max\left\{0, \langle C^L_{(\boldsymbol{x},E)}\rangle - \sqrt{\langle\left(C^L_{(\boldsymbol{x},E)} - \langle C^L_{(\boldsymbol{x},E)}\rangle\right)^2\rangle}\right\}, \tag{E4}$$

respectively, where $\sqrt{\langle(C^L_{(\boldsymbol{x},E)} - \langle C^L_{(\boldsymbol{x},E)}\rangle)^2\rangle}$ is the standard deviation. The reason for this definition, rather than just the standard deviation, is to avoid the suggestion that the local Chern number is anything other than 0 or 1 here. A symmetric error bar using only the standard deviation can suggest either $C^L_{(\boldsymbol{x},E)} < 0$ or $C^L_{(\boldsymbol{x},E)} > 1$, which it does not. As the disorder increases, the probability of finding a topologically nontrivial state inside the lattice decreases. In addition to the average value decreasing to zero, the variation (error bar width) increases.

Next, consider the coupling disorder. To create this, random numbers are added to the nonzero off-diagonal terms of δ_0 and δ_{10} in a symmetric fashion to preserve the Hermitian nature of $\delta H(t)$. Here we take random numbers r_j with mean zero, $\langle r_j\rangle = 0$, and standard deviation $\sqrt{\langle r_j^2\rangle} = \gamma J$, so that disorder strength is scaled relative to the hopping amplitude J. Each coupling is perturbed with a different random number. The three columns in Figs. 3, 7, and 10 correspond to $\gamma = 0.005,\ 0.02$, and 0.18, respectively.

Ensemble averages for the local Chern index are shown in Fig. 10 for the 0-gap ($E_0 = 0$) and π-gap ($E_\pi = \pi/T$). Again, the top and bottom error bars are defined by (E3) and (E4), respectively, to avoid the suggestion that they are greater than 1 or less than 0. Overall, the trend is similar to the on-site disorder: degradation of the chiral state as the intensity of disorder increases. That is, $\langle C^L_{(\boldsymbol{x},E)}\rangle \to 0$ as the disorder increases. We note the deterioration of the anomalous topological state from coupling disorder appears to occur earlier than

that of the on-site disorder. This would suggest that careful fabrication of the coupling coefficients in waveguide arrays is crucial for stable systems.

APPENDIX F: BULK-BOUNDARY CORRESPONDENCE IN THE SPECTRAL LOCALIZER FRAMEWORK

1. Bulk-boundary correspondence through the composite quadratic operator

In this section, we show how a bulk-boundary correspondence can be derived in the spectral localizer framework, guaranteeing the existence of boundary states at the interface between locally topological trivial and nontrivial regions.

The appearance of boundary states can be proven through another composite operator, the quadratic operator Q [50]. For a two-dimensional system with position operators X and Y, and effective Hamiltonian H_{F}, the quadratic operator is defined as

$$Q_{(x,y,E)}(X,Y,H_{\mathrm{F}}) = \kappa^2(X-xI)^2+\kappa^2(Y-yI)^2+(H_{\mathrm{F}}-EI)^2. \tag{F1}$$

The key reason to introduce this quadratic operator Q is that its associated quadratic local gap

$$\mu^{\mathrm{Q}}_{(\boldsymbol{x},E)}(\boldsymbol{X},H_{\mathrm{F}}) = \sqrt{\min[\mathrm{spec}(Q_{(\boldsymbol{x},E)}(\boldsymbol{X},H_{\mathrm{F}}))]} \tag{F2}$$

bounds the location and localization relative to the choice of $(\boldsymbol{x},E)$ of an approximate eigenstate across the input operators of Q, namely here the X, Y, and H_{F} operators. In particular, the quadratic gap $\mu^{\mathrm{Q}}_{(x,y,E)}$ at position (x,y) and energy E provide information about how much variance in X, Y, and H_{F} can be for a state centered (in a sense of the expectation value) at (x,y,E) [50]

$$\begin{aligned}\left(\mu^{\mathrm{Q}}_{(x,y,E)}(X,Y,H_{\mathrm{F}})\right)^2 = \min_{\phi\in\mathscr{H}}\Big\{&\kappa^2\Delta^2_\phi[X]+\kappa^2\left(\Delta^1_\phi[X]-x\right)^2\\ &+\kappa^2\Delta^2_\phi[Y]+\kappa^2\left(\Delta^1_\phi[Y]-y\right)^2\\ &+\Delta^2_\phi[H_{\mathrm{F}}]+\left(\Delta^1_\phi[H_{\mathrm{F}}]-E\right)^2\Big\},\end{aligned} \tag{F3}$$

where $\mathscr{H}$ is the system's Hilbert space, and $\Delta^2_\phi[M] = \langle\phi|M^2|\phi\rangle - \langle\phi|M|\phi\rangle^2$ and $\Delta^1_\phi[M] = \langle\phi|M|\phi\rangle$ correspond to the variance and mean value of the operator M, respectively. Notably the difference in the local gap obtained from the spectral localizer, μ^{C}, and the quadratic operator, μ^{Q}, are bounded as [50]

$$\begin{aligned}&\left|\left(\mu^{\mathrm{C}}_{(x,y,E)}(X,Y,H_{\mathrm{F}})\right)^2-\left(\mu^{\mathrm{Q}}_{(x,y,E)}(X,Y,H_{\mathrm{F}})\right)^2\right|\\ &\quad\leqslant \kappa\|[X,H_{\mathrm{F}}]\|+\kappa\|[Y,H_{\mathrm{F}}]\|.\end{aligned} \tag{F4}$$

Altogether, from Eq. (D4), a bulk-boundary correspondence naturally appears: at locations where the local topological invariant changes, the Clifford local gap μ^{C} must be zero, guaranteeing that the quadratic local gap μ^{Q} is small and therefore that there must be a nearby state of the system.

2. Quadratic operator for identifying localized states

As the local topological invariant in the spectral localizer framework can be defined irrespective of a well-defined bulk band gap [31,34,36], the latter means boundary states can also be predicted even if they are degenerate with the bulk spectrum. Here we show that while a real-space version of the bulk-boundary correspondence can be proved using the quadratic operators in the spectral localizer framework, the quadratic operator also provides a way to identify boundary states, including boundary states that are degenerate with bulk states [58,59].

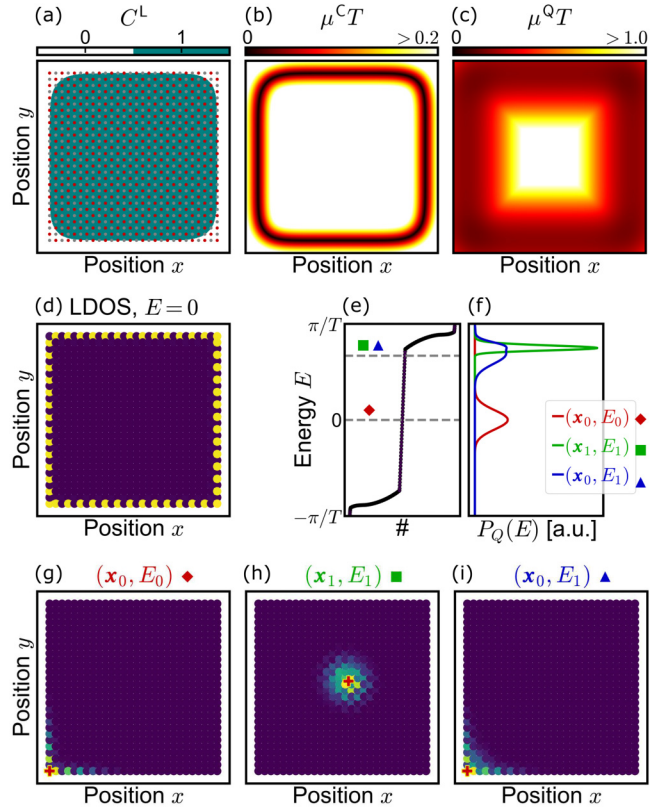

FIG. 11. (a) Local Chern number $C^{L}_{(\boldsymbol{x},E_0)}$ for the anomalous Floquet topological phase with coupling $J=5\pi/2T$ and at the center of the π-gap (here recentered to be at $E=0$); the white (teal) region denotes 0 (1). (b),(c) Clifford local gap $\mu^{\mathrm{C}}_{(\boldsymbol{x},E_0)}$ and quadratic local gap $\mu^{\mathrm{Q}}_{(\boldsymbol{x},E_0)}$ for this system. (d) Local density of states (LDOS) at $E=0$. (e) Spectrum of this system with open boundary conditions. (f) Projected density of states $P_Q(E)$. (g),(h),(i) Spatial distribution of $|\phi_\mu\rangle$ with a probe at $(\boldsymbol{x}_0,E_0)$, $(\boldsymbol{x}_1,E_1)$, and $(\boldsymbol{x}_0,E_1)$, respectively. The localizer and quadratic operators have been calculated with $\kappa=0.2/(Ta)$, period $T=1$[a.u.] and lattice constant $a=1$[a.u.], over a 28×28 lattice.

a. Boundary states

To begin, let us first consider the anomalous Floquet topological phase with coupling $J=5\pi/2T$ as in Fig. 1(f) in the main text, but with a 28×28 lattice. For this set of parameters, the system has well-defined bulk band gaps in the quasienergy bands and the spectrum of the system with open-boundary conditions is plotted in Fig. 11(e), where here the π-gap is centered at zero as explained in Appendix A. In that π-gap, the system is shown to be topologically nontrivial with nonzero local Chern numbers across the lattice as shown in Fig. 11(a), thus resulting in topological edge states at the

boundary of the lattice due to bulk-boundary correspondence. Because of the well-defined bulk band gap, those topological edge states can be easily visualized through the local density of states (LDOS) as shown in Fig. 11(d) at $E = 0$.

Nevertheless, as explained above, the local gap is also related to the location and localization of an approximate eigenstate of X, Y, and H_F. Here because the local Chern number changes values around the boundary of the lattice, the Clifford local gap μ^C must also be zero at those local invariant changes, as shown in Fig. 11(b). As the difference between the quadratic gap μ^Q and the Clifford gap μ^C is bounded [see Eq. (F4)], the quadratic gap must in turn have dips around the boundary of the lattice [see Fig. 11(c)]. Using Eq. (F3), we can see that the eigenstate $|\phi_\mu\rangle$ of the quadratic operator associated to the quadratic local gap $\mu^Q_{(x,y,E)}$ at some position (x, y) and energy E, namely the smallest eigenvalue of $Q_{(x,y,E)}(X, Y, H_F)$, corresponds to some states with minimal variance in X, Y, and H_F. In other words, the spatial distribution of the eigenstate $|\phi_\mu\rangle$ shows that it is localized around (x, y) with energy around E and the "projected" density of state (projected DOS) defined as

$$P_Q(E) = \sum_i |\langle\psi_i|\phi_\mu\rangle|^2 \delta(E - E_i), \tag{F5}$$

with $|\psi_i\rangle$ an eigenvector of H_F with eigenenergy E_i, gives the distribution across the eigenstate of the system's Floquet Hamiltonian H_F. For example, with a probe at a position on the boundary of the lattice $\boldsymbol{x}_0$ with an energy at the center of the π-gap E_0, the spatial distribution of $|\phi_\mu\rangle$ plotted in Fig. 11(g) clearly shows the topological edge state at the boundary of the lattice around $\boldsymbol{x}_0$ with some contribution from the other topological edge states in the π-gap around E_0, as illustrated by $P_Q(E)$ in Fig. 11(f). Similarly, with a probe in the bulk of the lattice $\boldsymbol{x}_1$ and energy close to the bulk bands E_1 display the bulk modes around $\boldsymbol{x}_1$ [Fig. 11(h)] with contribution from the other bulk modes around E_1 [Fig. 11(f)]. However, if we look at a position on the boundary of the lattice $\boldsymbol{x}_0$ with an energy E_1 close to both the bulk and edge bands, we can see the contribution of both bulk and boundary modes both in the spatial distribution of $|\phi_\mu\rangle$ [Fig. 11(i)] and more quantitatively in the projected DOS $P_Q(E)$ [Fig. 11(f)].

b. Boundary state resonances

When topological boundary states are degenerate with the bulk states, the quadratic operator can also be used to identify those states, which are here referred to as *boundary state resonances* as they are leaking into the bulk of the system. To provide a specific system that exemplifies such a case, let us consider a system that is in an anomalous Floquet topological phase with coupling $J = 5\pi/2T$ as in the previous subsection, but with disorder on the couplings, with standard deviation $0.85J$, everywhere except in the bottom left of the lattice. Because of the strong perturbation considered, several domains with different local topology appear throughout the lattice as classified by the local Chern number at $E = 0$ in Fig. 12(a), with one large topological domain in the bottom-left part of the lattice which corresponds to the region of no disorder. From bulk-boundary correspondence, topological boundary states are thus expected to appear at the interface between all

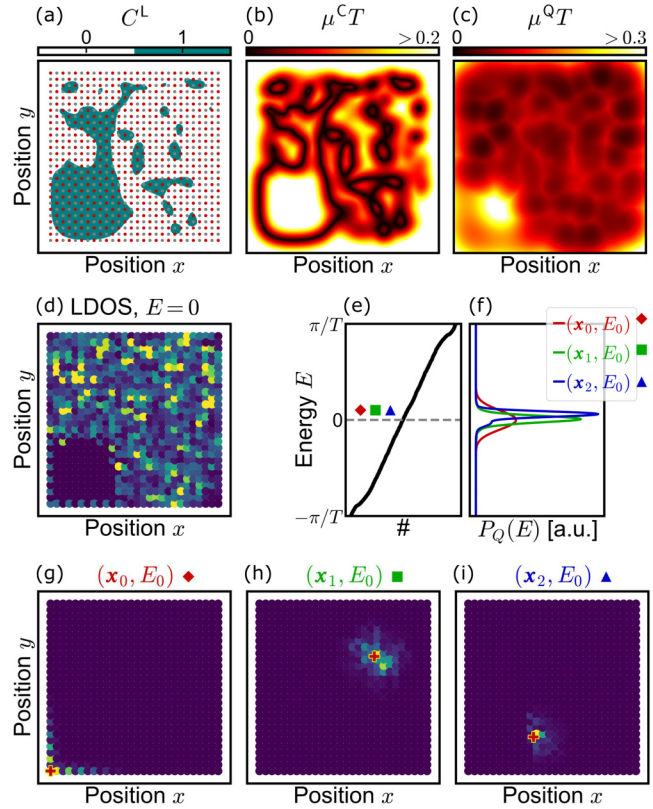

FIG. 12. (a) Local Chern number $C^L_{(\boldsymbol{x},E_0)}$ for the anomalous Floquet topological phase with coupling disorder around $J = 5\pi/2T$, with standard deviation $0.85J$, and at the center of the π-gap (here recentered to be at $E = 0$); the white (teal) region denotes 0 (1). (b),(c) Clifford local gap $\mu^C_{(\boldsymbol{x},E_0)}$ and quadratic local gap $\mu^Q_{(\boldsymbol{x},E_0)}$ for this system. (d) Local density of states (LDOS) at $E = 0$. (e) Spectrum of this system with open boundary conditions. (f) Projected density of states $P_Q(E)$. (g),(h),(i) Spatial distribution of $|\phi_\mu\rangle$ with a probe at $(\boldsymbol{x}_0, E_0)$, $(\boldsymbol{x}_1, E_1)$, and $(\boldsymbol{x}_0, E_1)$, respectively. The localizer and quadratic operators have been calculated with $\kappa = 0.2/(Ta)$, period $T = 1$[a.u.] and lattice constant $a = 1$[a.u.], over a 28×28 lattice.

of these topological and trivial domains. However, the spectrum of the system [Fig. 12(e)] is gapless in a sense that there is no clear energy range that only supports boundary states, such that the boundary states are degenerate with the bulk states. Therefore, an approach using the LDOS to visualize those boundary states will fail as those boundary states are also leaking into the bulk, as shown in Fig. 12(d).

Yet, looking at the associated local gap μ^C [Fig. 12(b)] and the quadratic local gap μ^Q [Fig. 12(c)] provides insight about the location of localized states at the corresponding energy E (here $E = 0$). For example, a probe at the bottom-left corner $\boldsymbol{x}_0$ reveals a boundary state along the boundary of the lattice [Fig. 12(g)] with contributions spanning several modes around $E = 0$ [Fig. 12(f)], resembling the example case of the previous subsection [Figs. 11(f) and 11(g)]. This is, in fact, expected as a zoom-in of this part of the lattice looks like the system with no disorder, resulting in the spatial distribution and projected DOS of $|\phi_\mu\rangle$ behaving as in the clean system with a defined bulk band gap. Meanwhile, a

probe located away from topological interfaces and in the bulk where there is disorders $\boldsymbol{x}_1$ reveals bulk states present at $E = 0$ [see Figs. 12(h) and 12(f)]. Notably, if we look at the position on a topological interface with the presence of disorders $\boldsymbol{x}_2$, the spatial distribution of $|\phi_\mu\rangle$ reveals the presence of the localized boundary state resonance [Fig. 12(i)] and the projected DOS shows a slightly different curve than the bulk states coming form the boundary state [Fig. 12(f)], demonstrating the contribution from both the bulk and boundary modes, namely leaky boundary states. Overall, at a given energy, the eigenstate $|\phi_\mu\rangle$ associated to the quadratic local gap μ^{Q} provides an indirect method to visualize the boundary states if the probe is at the boundary, as well as a quantitative measure of the system's eigenstate contribution.

APPENDIX G: USEFUL PROOFS ABOUT FLOQUET SYSTEMS

Consider the general solution of Eq. (1) given by $\mathbf{u}(t) = \Pi(t, t_0)\mathbf{u}_0$, where the principal matrix solution satisfies

$$\dot{\Pi}(t, t_0) = -iH(t)\Pi(t, t_0), \quad \Pi(t_0, t_0) = I.$$

The columns of $\Pi(t, t_0)$ correspond to linearly independent solutions of (1),

$$\Pi(t, t_0) = [\mathbf{u}_1(t)|\mathbf{u}_2(t)|\cdots|\mathbf{u}_n(t)].$$

The Hamiltonian $H(t)$ is assumed to be Hermitian, $H(t)^\dagger = H(t)$, where † denotes the transpose complex conjugate.

Lemma G1. If $H(t)$ is Hermitian, then the principal matrix solution $\Pi(t, t_0)$ is unitary.

Proof. Consider two linearly independent solutions of Eq. (1), $\mathbf{u}_a$(t) and $\mathbf{u}_b(t)$, such that

$$\dot{\mathbf{u}}_{a,b}(t) = -iH(t)\mathbf{u}_{a,b}(t).$$

These solutions form arbitrary columns of $\Pi(t, t_0)$. Then

$$\langle\dot{\mathbf{u}}_a|\mathbf{u}_b\rangle = i\langle\mathbf{u}_a|H(t)\mathbf{u}_b\rangle$$

and

$$\langle\mathbf{u}_a|\dot{\mathbf{u}}_b\rangle = -i\langle\mathbf{u}_a|H(t)\mathbf{u}_b\rangle.$$

Combining these reveals that $\frac{d}{dt}\langle\mathbf{u}_a|\mathbf{u}_b\rangle = 0$ for all t or $\langle\mathbf{u}_a(t)|\mathbf{u}_b(t)\rangle$ is constant. We set these to be orthogonal, i.e., $\langle\mathbf{u}_a(t)|\mathbf{u}_b(t)\rangle = 0$. Since these were arbitrary columns of the matrix solution, this implies that $\Pi(t, t_0)$ is unitary for all time, i.e., $\Pi(t, t_0)^\dagger\Pi(t, t_0) = I$. ■

The principal matrix solution of any Floquet system can be expressed as [41]

$$\Pi(t, t_0) = P(t, t_0)\exp[-i(t - t_0)H_{\mathrm{F}}], \tag{G1}$$

where exp denotes the matrix exponential. Since Π is unitary, the periodic matrix P is unitary and the matrix H_{F} is Hermitian.

Lemma G2. If $H(t)$ is Hermitian and periodic, then $P(t, t_0)$ is unitary and H_{F} is Hermitian.

Proof. Evaluation of Eq. (G1) at $t = t_0 + T$ reveals that the monodromy matrix is unitary

$$\|\exp(-iTH_{\mathrm{F}})\| = \|\Pi(t_0 + T, t_0)\| = 1,$$

since $P(t_0 + T, t_0) = I$ and $\Pi(t_0 + T, t_0)$ is unitary. As a result, the Floquet multipliers (eigenvalues) of $\exp(-iTH_{\mathrm{F}})$ lie on the unit circle. Hence the effective Hamiltonian matrix H_{F} is Hermitian. If two square matrices A, C are unitary and $A = BC$, then B is also unitary. As a result, the periodic matrix P is unitary and $P(t, t_0)^{-1} = P(t, t_0)^\dagger$. ■

[1] Z. Wang, Y. Chong, J. D. Joannopoulos, and M. Soljačić, Observation of unidirectional backscattering-immune topological electromagnetic states, Nature (London) **461**, 772 (2009).

[2] M. Hafezi, E. A. Demler, M. D. Lukin, and J. M. Taylor, Robust optical delay lines with topological protection, Nat. Phys. **7**, 907 (2011).

[3] M. Hafezi, S. Mittal, J. Fan, A. Migdall, and J. M. Taylor, Imaging topological edge states in silicon photonics, Nat. Photon. **7**, 1001 (2013).

[4] S. Klembt, T. H. Harder, O. A. Egorov, K. Winkler, R. Ge, M. A. Bandres, M. Emmerling, L. Worschech, T. C. Liew, M. Segev, C. Schneider, and S. Höfling, Exciton-polariton topological insulator, Nature (London) **562**, 552 (2018).

[5] T. Shintaku and T. Uno, Optical waveguide isolator based on nonreciprocal radiation, J. Appl. Phys. **76**, 8155 (1994).

[6] R. L. Espinola, T. Izuhara, M.-C. Tsai, R. M. Osgood, and H. Dötsch, Magneto-optical nonreciprocal phase shift in garnet/silicon-on-insulator waveguides, Opt. Lett. **29**, 941 (2004).

[7] B. Bahari, A. Ndao, F. Vallini, A. El Amili, Y. Fainman, and B. Kanté, Nonreciprocal lasing in topological cavities of arbitrary geometries, Science **358**, 636 (2017).

[8] V. Dal Lago, M. Atala, and L. E. F. Foa Torres, Floquet topological transitions in a driven one-dimensional topological insulator, Phys. Rev. A **92**, 023624 (2015).

[9] D. Leykam, M. C. Rechtsman, and Y. D. Chong, Anomalous topological phases and unpaired dirac cones in photonic Floquet topological insulators, Phys. Rev. Lett. **117**, 013902 (2016).

[10] Z. Yan, B. Li, X. Yang, and S. Wan, A general time-periodic driving approach to realize topological phases in cold atomic systems, Sci. Rep. **5**, 16197 (2015).

[11] K. Fang and Y. Wang, Anomalous quantum Hall effect of light in bloch-wave modulated photonic crystals, Phys. Rev. Lett. **122**, 233904 (2019).

[12] J. Lu, L. He, Z. Addison, E. J. Mele, and B. Zhen, Floquet topological phases in one-dimensional nonlinear photonic crystals, Phys. Rev. Lett. **126**, 113901 (2021).

[13] Q. Cheng, Y. Pan, H. Wang, C. Zhang, D. Yu, A. Gover, H. Zhang, T. Li, L. Zhou, and S. Zhu, Observation of anomalous π modes in photonic Floquet engineering, Phys. Rev. Lett. **122**, 173901 (2019).

[14] M. C. Rechtsman, J. M. Zeuner, Y. Plotnik, Y. Lumer, D. Podolsky, F. Dreisow, S. Nolte, M. Segev, and A. Szameit, Photonic Floquet topological insulators, Nature (London) **496**, 196 (2013).

[15] M. J. Ablowitz and J. T. Cole, Tight-binding methods for general longitudinally driven photonic lattices: Edge states and solitons, Phys. Rev. A **96**, 043868 (2017).

[16] L. J. Maczewsky, J. M. Zeuner, S. Nolte, and A. Szameit, Observation of photonic anomalous Floquet topological insulators, Nat. Commun. **8**, 13756 (2017).

[17] J. Guglielmon, S. Huang, K. P. Chen, and M. C. Rechtsman, Photonic realization of a transition to a strongly driven Floquet topological phase, Phys. Rev. A **97**, 031801(R) (2018).

[18] M. J. Ablowitz and J. T. Cole, Topological insulators in longitudinally driven waveguides: Lieb and kagome lattices, Phys. Rev. A **99**, 033821 (2019).

[19] S. K. Ivanov, Y. Zhang, Y. V. Kartashov, and D. V. Skryabin, Floquet topological insulator laser, APL Photon. **4**, 126101 (2019).

[20] S. Mukherjee and M. C. Rechtsman, Observation of Floquet solitons in a topological bandgap, Science **368**, 856 (2020).

[21] L. J. Maczewsky, M. Heinrich, M. Kremer, S. K. Ivanov, M. Ehrhardt, F. Martinez, Y. V. Kartashov, V. V. Konotop, L. Torner, D. Bauer, and A. Szameit, Nonlinearity-induced photonic topological insulator, Science **370**, 701 (2020).

[22] L. J. Maczewsky, B. Höckendorf, M. Kremer, T. Biesenthal, M. Heinrich, A. Alvermann, H. Fehske, and A. Szameit, Fermionic time-reversal symmetry in a photonic topological insulator, Nat. Mater. **19**, 855 (2020).

[23] L. He, Z. Addison, J. Jin, E. J. Mele, S. G. Johnson, and B. Zhen, Floquet Chern insulators of light, Nat. Commun. **10**, 4194 (2019).

[24] J. Cayssol, B. Dóra, F. Simon, and R. Moessner, Floquet topological insulators, Phys. Status Solidi RRL **7**, 101 (2013).

[25] M. S. Rudner, N. H. Lindner, E. Berg, and M. Levin, Anomalous edge states and the bulk-edge correspondence for periodically driven two-dimensional systems, Phys. Rev. X **3**, 031005 (2013).

[26] F. Nathan and M. S. Rudner, Topological singularities and the general classification of Floquet–Bloch systems, New J. Phys. **17**, 125014 (2015).

[27] F. Harper, R. Roy, M. S. Rudner, and S. Sondhi, Topology and broken symmetry in Floquet systems, Annu. Rev. Condens. Matter Phys. **11**, 345 (2020).

[28] R. Roy and F. Harper, Periodic table for Floquet topological insulators, Phys. Rev. B **96**, 155118 (2017).

[29] P. Titum, N. H. Lindner, M. C. Rechtsman, and G. Refael, Disorder-Induced Floquet topological insulators, Phys. Rev. Lett. **114**, 056801 (2015).

[30] P. Titum, E. Berg, M. S. Rudner, G. Refael, and N. H. Lindner, Anomalous Floquet-Anderson insulator as a nonadiabatic quantized charge pump, Phys. Rev. X **6**, 021013 (2016).

[31] A. Cerjan and T. A. Loring, Local invariants identify topology in metals and gapless systems, Phys. Rev. B **106**, 064109 (2022).

[32] A. Cerjan and T. A. Loring, An operator-based approach to topological photonics, Nanophotonics **11**, 4765 (2022).

[33] A. Cerjan, T. A. Loring, and H. Schulz-Baldes, Local markers for crystalline topology, Phys. Rev. Lett. **132**, 073803 (2024).

[34] K. Y. Dixon, T. A. Loring, and A. Cerjan, Classifying topology in photonic heterostructures with gapless environments, Phys. Rev. Lett. **131**, 213801 (2023).

[35] S. Wong, T. A. Loring, and A. Cerjan, Probing topology in nonlinear topological materials using numerical k-theory, Phys. Rev. B **108**, 195142 (2023).

[36] S. Wong, T. A. Loring, and A. Cerjan, Classifying topology in photonic crystal slabs with radiative environments, npj Nanophoton. **1**, 19 (2024).

[37] T. A. Loring, K-Theory and pseudospectra for topological insulators, Ann. Phys. (N.Y.) **356**, 383 (2015).

[38] H. Liu and I. C. Fulga, Mixed higher-order topology: Boundary non-Hermitian skin effect induced by a Floquet bulk, Phys. Rev. B **108**, 035107 (2023).

[39] Z. Qi, I. Na, G. Refael, and Y. Peng, Real-space topological invariant for time-quasiperiodic Majorana modes, Phys. Rev. B **110**, 014309 (2024).

[40] L. P. Gavensky, G. Usaj, and N. Goldman, Streda formula for Floquet systems: Topological invariants and quantized anomalies from Cesaro summation, Phys. Rev. X **15**, 031067 (2025).

[41] G. Teschl, *Ordinary Differential Equations and Dynamical Systems*, Grad. Studies in Math. Vol. 140 (AMS, Providence, RI, 2010).

[42] T. A. Loring and F. Vides, Computing Floquet Hamiltonians with symmetries, J. Math. Phys. **61**, 113501 (2020).

[43] A. Altland and M. R. Zirnbauer, Nonstandard symmetry classes in mesoscopic normal-superconducting hybrid structures, Phys. Rev. B **55**, 1142 (1997).

[44] A. P. Schnyder, S. Ryu, A. Furusaki, and A. W. W. Ludwig, Classification of topological insulators and superconductors in three spatial dimensions, Phys. Rev. B **78**, 195125 (2008).

[45] A. Kitaev, Periodic table for topological insulators and superconductors, AIP Conf. Proc. **1134**, 22 (2009).

[46] S. Ryu, A. P. Schnyder, A. Furusaki, and A. W. W. Ludwig, Topological insulators and superconductors: Tenfold way and dimensional hierarchy, New J. Phys. **12**, 065010 (2010).

[47] T. Loring and H. Schulz-Baldes, The spectral localizer for even index pairings, J. Noncommutat. Geom. **14**, 1 (2020).

[48] A. Kitaev, Anyons in an exactly solved model and beyond, Ann. Phys. (N.Y.) **321**, 2 (2006).

[49] E. Fel'dman, On the convergence of the magnus expansion for spin systems in periodic magnetic fields, Phys. Lett. A **104**, 479 (1984).

[50] A. Cerjan, T. A. Loring, and F. Vides, Quadratic pseudospectrum for identifying localized states, J. Math. Phys. **64**, 023501 (2023).

[51] R. Bhatia, *Matrix Analysis*, Graduate Texts in Mathematics Vol. 169 (Springer New York, New York, 1997).

[52] L. Peletan, S. Baguet, M. Torkhani, and G. Jacquet-Richardet, A comparison of stability computational methods for periodic solution of nonlinear problems with application to rotordynamics, Nonlin. Dyn. **72**, 671 (2013).

[53] F. N. Ünal, B. Seradjeh, and A. Eckardt, How to directly measure Floquet topological invariants in optical lattices, Phys. Rev. Lett. **122**, 253601 (2019).

[54] R. Asapanna, R. E. Sokhen, A. F. Adiyatullin, C. Hainaut, P. Delplace, Á. Gómez-León, and A. Amo, Observation of extrinsic topological phases in Floquet photonic lattices, arXiv:2412.14324.

[55] F. Nathan, M. S. Rudner, N. H. Lindner, E. Berg, and G. Refael, Quantized magnetization density in periodically driven systems, Phys. Rev. Lett. **119**, 186801 (2017).

[56] K. W. Kim, D. Bagrets, T. Micklitz, and A. Altland, Quantum Hall criticality in Floquet topological insulators, Phys. Rev. B **101**, 165401 (2020).

[57] A. K. Ghosh, R. Arouca, and A. M. Black-Schaffer, Local and energy-resolved topological invariants for Floquet systems, Phys. Rev. B **110**, 245306 (2024).

[58] A. Sagiv and M. I. Weinstein, Effective gaps in continuous Floquet Hamiltonians, SIAM J. Math. Anal. **54**, 986 (2022).

[59] S. N. Hameedi, A. Sagiv, and M. I. Weinstein, Radiative decay of edge states in Floquet media, Multiscale Model. Simul. **21**, 925 (2023).